Physica D 472 (2025) 134475

Contents lists available at ScienceDirect

Physica D

journal homepage: www.elsevier.com/locate/physd

Minimal model for investigation of noise-induced bubbling

Viktor Avrutin [a,*], Zhanybai T. Zhusubaliyev [b,c], Kuntal Mandal [d], Frank Bastian [e], Abdelali El Aroudi [d]

[a] Institute for Systems Theory and Automatic Control, University of Stuttgart, Germany
[b] Department of Computer Science, Dynamics of Non-Smooth Systems International Scientific Laboratory, Southwest State University, Kursk, Russia
[c] Institute of Mathematics, Physics, Engineering and Information Technologies, Osh State University, Osh, Kyrgyzstan
[d] Departament d'Enginyeria Electrònica, Elèctrica i Automàtica, Universitat Rovira i Virgili, Tarragona, Spain
[e] School of Mathematical Sciences, University College Cork, Ireland

ARTICLE INFO

Communicated by Tamas Insperger

Keywords:
Bubbling
Fast-scale bifurcations
Noise amplification
Power converters
Non-autonomous maps

ABSTRACT

The term 'bubbling' refers to the phenomenon where high-frequency oscillations appear abruptly within a restricted phase range, distorting the signal waveform in various power electronic applications. Recent investigations suggest that this phenomenon may be triggered not by changes in the topology of underlying invariant sets but rather by an extreme amplification of disturbances, attributable to noise in physical experiments and rounding errors in simulations.

This work proposes a minimal (archetypal) model to investigate this phenomenon. The primary purpose of this model is to predict how various parameters of the underlying system influence noise-induced bubbling. The model's predictions were verified through physical experiments, which confirmed that an increase in the noise level can trigger the occurrence of bubbling, as expected. Moreover, the same effect can be caused by an increase in the frequency modulation ratio, contrary to established expectations.

1. Introduction

Bifurcation theory mainly studies how various invariant sets may undergo topological transformations. Examples of such transformations include the appearance and disappearance of solutions, as well as several re-configurations of their stable and unstable manifolds. However, in an applied context, not only topological but also geometrical transformations can hold significance. An impressive example of this is the phenomenon known as bubbling.

In the realm of power electronics, numerous systems require signals with minimal harmonic distortion in order to function optimally [1,2]. However, it has been frequently observed that under some conditions, these signals become disrupted, leading to undesirable outcomes. The specific type of disruption, discussed in the present study, manifests as high-frequency, low-amplitude oscillations observable within a restricted phase interval of a slowly oscillating signal. This phenomenon is termed bubbling because the signal's local minima and maxima resemble a bubble within the affected phase interval. It has been conjectured that the onset of bubbling is caused by a bifurcation, called a fast-scale bifurcation, owing to its connection with the appearance of an additional high-frequency component in the signal.

Over the last two decades, the bubbling phenomenon has been observed both experimentally and numerically in several kinds of power electronics circuits, such as DC-DC converters [3], AC-DC rectifiers [4–10], and DC-AC inverters [11–17]. However, no completely convincing explanation of the mechanism triggering the onset of bubbling has been proposed in these publications. Several authors [3,4,11,18] have noted that bubbling often appears after a bifurcation related to eigenvalues crossing the unit circle, such as flip, pitchfork or Neimark–Sacker bifurcation. Consequently, it has been commonly assumed that bubbling is caused by these bifurcations, although the specific mechanism generating high-frequency oscillations within a restricted phase interval remained unidentified. Moreover, the factors determining the phase interval affected by bubbling remained unknown as well.

In our recent work [19], we reported the onset of bubbling in a model of a DC-AC inverter at parameter values where the system cannot exhibit any bifurcations related to eigenvalues crossing the unit circle. Using an approach based on geometric properties of invariant sets rather than on topological considerations, we explained the mechanism leading to the onset of bubbling both for the cases previously reported (i.e., associated with a bifurcation) and for the case that it occurs independently of any bifurcations.

---

[*] Corresponding author.
E-mail addresses: Viktor.Avrutin@ist.uni-stuttgart.de (V. Avrutin), Zhanybai@hotmail.com (Z.T. Zhusubaliyev), kuntal.mandal@urv.cat (K. Mandal), FBastian@ucc.ie (F. Bastian), abdelali.elaroudi@urv.cat (A. El Aroudi).

https://doi.org/10.1016/j.physd.2024.134475
Received 13 March 2024; Received in revised form 20 November 2024; Accepted 29 November 2024

In essence, the explanation reported in [19] can be summarized as follows. As a first step, we identified regions in the state space such that an orbit located inside these regions (called non-bubbling intervals in the state space) at any phase does not exhibit bubbling. Thus, bubbling occurs in the phase interval where the points of an orbit leave the non-bubbling interval in the state space. Naturally, this prompts the question of why an orbit would leave these intervals? It turns out that this can happen due to various causes.

One of these causes is the displacement of solutions appearing at a bifurcation related to eigenvalues crossing the unit circle. This indicated that in the previously reported cases, the onset of bubbling takes place not exactly at the bifurcation point but slightly after. Another reason leading to the same effect is the displacement of an orbit after a border collision bifurcation, as discussed in [20]. However, in the present work, we focus on a different mechanism causing orbits to leave non-bubbling intervals in the state space, triggering the onset of bubbling. This mechanism is unrelated to any bifurcation and is based on the amplification of noise in a specific phase interval due to expanding functions governing the system's dynamics.

Since noise is inherent in physical experiments and numerical simulations are also affected by disturbances (e.g. rounding errors), which can be considered numerical noise, a paradoxical situation may arise when considering a noise-free model. In such cases, the exact solution to the model does not exhibit bubbling, yet both signals obtained by experiments involving the physical setup as well as by numerical simulations of the model manifest bubbling. For more details on this phenomenon, referred to as noise-induced bubbling, we refer to [20].

Building upon the theory presented in [19,20], in the present paper we ask the question of how the onset of noise-induced bubbling depends on several properties of the systems exhibiting this phenomenon. To provide a possibly general answer to this question, we propose the following approach. Rather than focusing on specific circuit models, we develop a generic model that incorporates the essential properties relevant to bubbling occurrence. The idea behind this approach is to provide a tool acting as kind of "common denominator" for several applied systems where this phenomenon occurs, regardless of their specific origin. For this reason, we call this model an *archetypal model* designed for investigating noise-induced bubbling.

The remainder of this paper is organized as follows. In Section 2 we provide a brief description of the inverter system exhibiting the noise-induced bubbling phenomenon, already discussed in [19,20]. In Section 3, we recall the properties of the model relevant for the onset of bubbling. In Section 4 we set up the archetypal model proposed for the investigation of the bubbling phenomenon. Thereafter, in Section 5 we demonstrate how this phenomenon is influenced by several parameters. An experimental confirmation of the obtained result is presented in Section 6. Eventually, Section 7 concludes.

2. Full model

2.1. Description of the converter

In [19], we investigated the bubbling phenomenon in an H-bridge DC-AC inverter with inductor current feedback and fixed frequency pulse width modulation (PWM). A schematic diagram of this inverter is shown in Fig. 1. Here, E_0 represents the *DC* voltage and $i(t)$ is the load current. R and L are the resistive and inductive components of the load. The switches $S_1 - S_4$ are controlled by a sinusoidal pulse-width modulated signal. The switches operate in pairs such that S_1 and S_4 are ON when S_2 and S_3 are OFF, and vice versa. When S_1, S_4 are ON and S_2, S_3 are OFF, a positive voltage E_0 will be applied to the RL-load; and when S_1, S_4 are OFF and S_2, S_3 are ON, this voltage is reversed.

In order to generate the switching signal to $S_1 - S_4$, the corrector amplifier DA_2 first produces the control signal $\xi(t) = \alpha(V_{\text{ref}}(t) - (\beta V_{\text{out}} + V_N))$ that measures the difference between the reference voltage $V_{\text{ref}}(t) = V_m \cos\left(\frac{2\pi}{ma}t\right)$ and the output voltage $\beta V_{\text{out}}(t) = \beta i(t) R$ of the load voltage sensor with sensitivity parameter β. Here, α is the corrector gain factor; a denotes the ramp period (the period of the clock signal V_{clock}) and m is referred to as the frequency modulation ratio. This number is assumed to be integer. As for V_{N}, it represents an additional noise signal applied to the considered circuit in the experimental setup in order to investigate its functioning under varying noise levels, as described in Section 6.

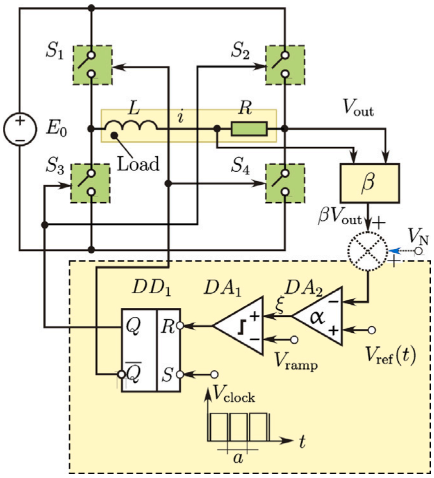

Fig. 1. Schematic representation of the considered H-bridge DC/AC power converter with PWM feedback control of the second kind.

The modulator implements pulse width modulation of the second kind (PWM-2). Note that the PWM-2 is designed in such a way, that apart from the switching at the beginning of each ramp cycle, at most one switching takes place during one period of ramp cycle. This is guaranteed by the flip-flop DD_1 and is necessary because multiple switchings during one ramp period may lead to sliding and other undesired phenomena, as demonstrated in [21].

The flip-flop DD_1 is set to the logic level "1" by the clock signal V_{clock} at the beginning of every ramp period a, regardless of the value of the control signal $\xi(t)$. In this case, the switches S_1, S_4 are switched ON and S_2, S_3 are OFF. The control signal $\xi(t)$ is compared by the comparator DA_1 with a saw-tooth wave form $V_{\text{ramp}}(t) = 2V_0(t/a - \lfloor t/a \rfloor - 1/2)$. As soon as the ramp voltage exceeds the value of the control signal $\xi(t)$, the output of the control flip-flop DD_1 is set to the logic level "0" and the switches S_1, S_4 are turned OFF, while S_2, S_3 are turned ON. The ramp function $V_{\text{ramp}}(t)$ varies between $+V_0$ and $-V_0$ in synchrony with the clock signal. If $\xi(t) > V_{\text{ramp}}(t)$ or $\xi(ka) < -V_0$ in the whole ramp period, the modulator is saturated. Then, the duration of the positive pulse is equal to the ramp period in the former case, and to zero in the latter one.

2.2. Normalized model in continuous time

Let us introduce the dimensionless dynamic variable $x = \dfrac{Ri}{E_* \varGamma} = \dfrac{Ri}{E_0}$ and the following set of dimensionless parameters:

$$P = \frac{V_0}{\beta E_*}, \; q = \frac{V_m}{\beta E_*}, \; \varGamma = \frac{E_0}{E_*}.$$

The parameter P controls the amplitude of the ramp function, q represents the amplitude of the reference voltage, and $\varGamma$ represents the DC source voltage, all normalized with respect to $E_* = 1.0$ V. In these terms, the dynamics of the converter described by the following differential equation with a discontinuous right hand side:

$$\frac{dx}{dt} = \lambda_*(x - \mathrm{K_F}), \; \lambda_* = -\frac{R}{L}. \tag{1}$$

Here the parameter λ_* has a dimension s^{-1}. In order to normalize this parameter (i.e. make it dimensionless) we introduce the dimensionless time variable $\tau = t/a$. Since

$$\frac{dx}{dt} = \frac{dx}{d\tau}\cdot\frac{d\tau}{dt} = \frac{\dot{x}}{a},\quad \dot{x} = \frac{dx}{d\tau},\quad \frac{d\tau}{dt} = 1/a,$$

Eq. (1) can be rewritten in the dimensionless form

$$\dot{x} = \lambda(x - \mathrm{K_F}(\tau,\varphi)),\ \lambda = \lambda_* a = -\frac{R}{L}\cdot a. \tag{2}$$

The switching function $\mathrm{K_F}$ takes the values ±1 depending on τ and φ. The values $\mathrm{K_F} = +1$ and $\mathrm{K_F} = -1$ correspond to the output of DD_1 equal to the logic level "1" and "0", respectively.

The switching function $\mathrm{K_F}$ during the kth normalized ramp cycle $k < \tau < k+1$, $k = 0, 1, 2, \ldots$ is given by

$$\mathrm{K_F} = \begin{cases} +1, & \text{if } k < \tau \leqslant \tau_k; \\ -1, & \text{if } \tau_k < \tau \leqslant k+1, \end{cases}$$

where the switching time τ_k is determined as the first time at which the function

$$\varphi(\tau) = \frac{q}{\Gamma}\cos\left(\frac{2\pi\tau}{ma}\right) - x(\tau) - \eta(\tau),$$

$$\eta(\tau) = \frac{2P}{\alpha\Gamma}(\tau - \lfloor\tau\rfloor - 1/2),\quad \lfloor\tau\rfloor = k,\ k = 0, 1, 2, \ldots.$$

crosses zero from a positive to a negative value, if the modulator is not saturated (see below).

2.3. Normalized model in discrete time

Within the time interval $k < \tau \leqslant \tau_k$, the function $\mathrm{K_F}$ takes the value +1 and Eq. (2) is given by $\dot{x} = \lambda(x-1)$. From its solution

$$x(\tau) = \mathrm{e}^{\lambda(\tau-k)}(x_k - 1) + 1$$

to the initial condition $x_k = x(\tau)|_{\tau=k}$, we obtain at the switching time $\tau = \tau_k$ the value

$$x(\tau_k) = \mathrm{e}^{\lambda(\tau_k-k)}(x_k - 1) + 1. \tag{3}$$

In the subsequent time interval $\tau_k < \tau \leqslant k+1$, Eq. (2) has the form $\dot{x} = \lambda(x+1)$. Its solution

$$x(\tau) = \mathrm{e}^{\lambda(\tau-\tau_k)}(x(\tau_k) + 1) - 1$$

to the initial value given by Eq. (3) implies that for $\tau = k+1$ we have

$$x_{k+1} = \mathrm{e}^{\lambda}(x_k - 1) + 2\mathrm{e}^{\lambda(1-z_k)} - 1. \tag{4}$$

Here, z_k is the pulse duration ($0 \leqslant z_k \leqslant 1$), determined by

$$z_k = \begin{cases} 0, & \text{if } \varphi_k(0) \leqslant 0; \\ z_k^*, & \text{if } \varphi_k(0) > 0 \text{ and } \varphi_k(1) < 0; \\ 1, & \text{if } \varphi_k(1) \geqslant 0, \end{cases}$$

where z_k^* is the smallest non-negative root to the equation

$$\begin{aligned} \varphi_k(z_k) = &\frac{q}{\Gamma}\cos\left(\frac{2\pi(z_k+k)}{ma}\right) - 1 - (x_k - 1)\,\mathrm{e}^{\lambda z_k} \\ &- \frac{2P}{\alpha\Gamma}(z_k - 1/2) = 0. \end{aligned} \tag{5}$$

The cases $z_k = 0$ and $z_k = 1$ correspond to the saturation of the modulator which occur if

$$\varphi_k(0) = \frac{q}{\Gamma}\cos\left(\frac{2\pi k}{ma}\right) - x_k + \frac{P}{\alpha\Gamma} \leqslant 0$$

$$\varphi_k(1) = \frac{q}{\Gamma}\cos\left(\frac{2\pi(k+1)}{ma}\right) - 1 - (x_k - 1)\,\mathrm{e}^{\lambda} - \frac{P}{\alpha\Gamma} \geqslant 0,$$

respectively.

Summing up, we obtain the discrete-time model (stroboscopic mapping) of the considered system, given by the following piecewise smooth non-autonomous 1D map:

$$x_{k+1} = g(x_k, k), \tag{6a}$$

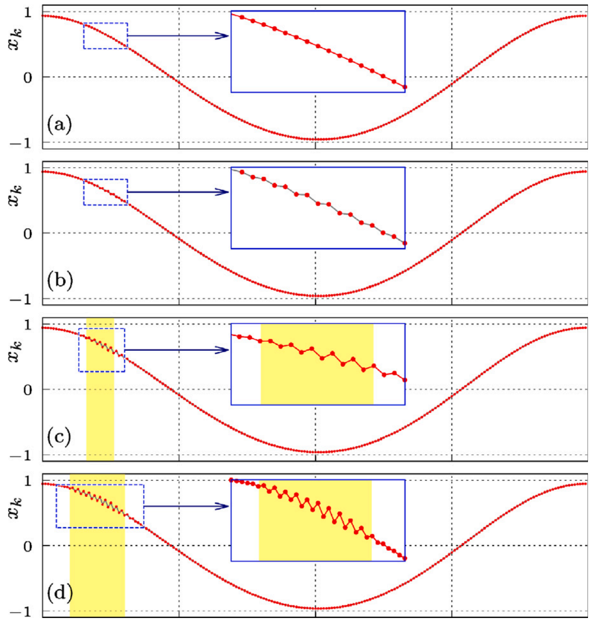

Fig. 2. Orbits of map (6) calculated numerically using standard double precision for (a) $\alpha = 9.0$; (b) $\alpha = 10.0$; (c) $\alpha = 10.205$; (d) $\alpha = 10.5$. In (c), (d), bubbling-affected phase intervals are highlighted.

$$g(x,k) = \begin{cases} g^{\mathcal{L}}(x,k) & = b(x-1)+1 \\ & \quad\text{if } x \in \mathcal{I}_{\mathcal{L}}; \\ g^{\mathcal{M}}(x,k) & = b(x-1) + 2b^{1-z_k} - 1 \\ & \quad\text{if } x \in \mathcal{I}_{\mathcal{M}}; \\ g^{\mathcal{R}}(x,k) & = b(x+1)-1 \\ & \quad\text{if } x \in \mathcal{I}_{\mathcal{R}}, \end{cases} \tag{6b}$$

with $b = \mathrm{e}^{\lambda}$. Here, the partitions

$$\begin{aligned} \mathcal{I}_{\mathcal{L}} &= \{(x,k) \mid x \leqslant s^-(k)\}, \\ \mathcal{I}_{\mathcal{M}} &= \{(x,k) \mid s^-(k) < x < s^+(k)\}, \\ \mathcal{I}_{\mathcal{R}} &= \{(x,k) \mid x \geqslant s^+(k)\} \end{aligned} \tag{6c}$$

are separated from each other by the borders

$$s^-(k) = \left\{(x,k) \mid x = \frac{q}{\Gamma b}c_{k+1} + 1 - \frac{1}{b} - \frac{P}{\alpha\Gamma b}\right\}$$

$$s^+(k) = \left\{(x,k) \mid x = \frac{q}{\Gamma}c_k + \frac{P}{\alpha\Gamma}\right\}$$

where

$$c_k = \cos\left(\frac{2\pi k}{m}\right),\quad c_{k+1} = \cos\left(\frac{2\pi(k+1)}{m}\right) \tag{6d}$$

and the value z_k is determined by Eq. (5) as described above.

The desired operational regime of the inverter corresponds to an attracting m-cycle of map (6) where m is the parameter representing the frequency modulation ratio, i.e. the ratio between the high switching frequency and the low sinusoidal signal reference frequency.

In the applied context, a good quality of the inverter's output signal is associated with a possibly low value of its total harmonic distortion. To achieve such a low value, the frequency modulation ratio m has to be sufficiently high, since this decreases the switching ripple amplitude and hence maintains the harmonic distortion at sufficiently low level. The value of m ranges from 9 (odd multiple of 3) for high power applications to several thousands for low power cases.

Examples of m-cycles, $m = 200$, obtained numerically by forward iterations of map (6) using a standard double precision number representation are shown in Fig. 2. The cycle shown in Fig. 2(a) corresponds to the desired operational regime of the inverter as evidenced by its points aligning with a smooth sinusoidal curve without any visible disruptions. However, as illustrated in Figs. 2(b), (c), (d), under parameter variation, the cycles become more and more disrupted in the phase interval at the beginning of the down-slope of the signal. Initially, this disruption is weak (see a slight deformation of the waveform well-recognizable in the inset in Fig. 2(b)). Then, under subsequent parameter variation, the disruption becomes stronger, resulting in well-visible high frequency oscillations (Fig. 2(c), (d)) signifying the onset of bubbling. It can be easily verified that this onset has no relation to eigenvalues crossing the unit circle, since the multipliers of all four cycles shown Fig. 2 are near zero in magnitude. This raises the question of the underlying mechanism leading to the onset of bubbling in the considered system.

3. Bubbling phenomenon

By definition, the bubbling phenomenon manifests itself as high-frequency, low amplitude oscillations visible in a restricted phase interval of a signal. For convenience, we define a point x_k of a signal to be *bubbling-affected* if it represents a local minimum or maximum of the signal [22]. In this sense, only the waveforms shown in Fig. 2(c) and (d) exhibit bubbling in the highlighted phase intervals consisting of such points. For short, these intervals are referred to as *bubbling-affected phase intervals*. Note also that the waveform shown in Fig. 2(b) does not exhibit bubbling in the sense of the definition given above, but a weaker form of disruption. In [19], it has been shown that this form of disruption, denoted as *simmering*, represents bubbling of the first forward differences of the signal (a kind of its derivative with respect to the discrete time variable). As for the waveform shown in Fig. 2(a), it exhibits neither bubbling nor simmering, but its forward differences of higher ranks might be still affected by high frequency oscillations [20].

In [19], we demonstrated that the appearance of bubbling-affected phase intervals can be explained by a purely geometric approach. Indeed, for a given phase k, we detected a specific state space interval $\mathcal{I}_k$ such that if an actual point x_k is located outside this intervals, it is bubbling-affected. Moreover, we identified a series of (typically nested) phase space intervals related to weaker distortions of the signals (such as simmering or even weaker forms). It has already been noticed in [19] that expanding functions may cause an orbit to enter first simmering- and eventually bubbling-affected intervals in the state space. However, the mechanism causing the initial disturbance to occur was not explained in the cited work.

The next step towards understanding the bubbling phenomenon has been presented in [20] where we have shown that there are several different reasons for the initial disturbance leading to bubbling. The simplest and most unexpected of these reasons is the presence of noise, which leads to a phenomenon we call noise-induced bubbling. To explain this phenomenon, let us consider first an m-cycle $\mathcal{O}_m$ of some 1D map f with the points $x_0, \dots, x_{m-1}$. A sufficient condition for this cycle to be stable is that its multiplier given by $\lambda(\mathcal{O}_m) = \prod_{k=0}^{m-1} f'_k(x_k)$ satisfies $|\lambda(\mathcal{O}_m)| < 1$. However, it is worth noticing that the stability of the overall cycle $\mathcal{O}_m$ does not imply a local stability of its individual points, determined by the value of the derivative f' at these points. A point x_k of the cycle $\mathcal{O}_m$ is referred to as *contractive* if $|f'_k(x_k)| < 1$ and as *expanding* if $|f'_k(x_k)| > 1$. In general, contractive and expanding points of a cycle can be mixed arbitrarily, and indeed, in many cases a few expanding points are followed by a contractive one, which compensate their local instability. However, the main distinguishing feature of cycles considered in [19,20] as well as in the present work is that contractive and expanding points are sorted in specific way such that the compensatory effect does not act over long phase intervals of these cycles. More precisely, we assume that there are two numbers i, j with $0 \leqslant i < j \leqslant m-1$ such that the points $x_i, \dots, x_{j-1}$ are expanding and the points $x_j, \dots, x_{m-1}, x_0, \dots, x_{i-1}$ are contractive. Denoting the index k of the point x_k as its phase, we call, for short, the interval $[i, j-1]$ the *expanding phase interval* of the cycle $\mathcal{O}_m$ and $[j, i-1]$ its *contractive phase interval*. Note that when dealing with m-cycles and phase intervals $[j, \ell]$ with $j > \ell$, we adopt the natural notation $[j, \ell] = [j, m-1] \cup [0, \ell]$.

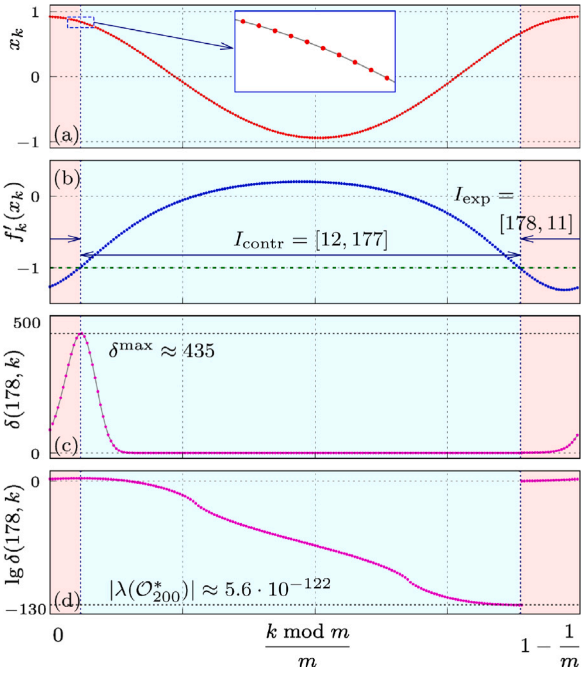

Fig. 3. (a) A non-bubbling 200-cycle $\mathcal{O}_{200}$ at $\alpha = 7.0$; (b) the corresponding values of the derivatives f'_k evaluated at the points of the cycle; (c) CPAF calculated starting from the beginning of the expanding phase interval. (d) logarithmic representation of the CPAF. In all four figures, the contractive and expanding phase intervals are indicated.

As an example, Fig. 3 shows contractive and expanding phase intervals of a non-bubbling 200-cycle presented in Fig. 3(a). Since the values $f'_k(x_k)$ are above -1 for $12 \leqslant k \leqslant 177$, the contractive phase interval of the considered cycle is $I_{\rm contr} = [12, 177]$. Similarly, the expanding phase interval of the cycle is $I_{\rm contr} = [178, 11] \equiv [0, 11] \cup [178, 199]$.

To quantify the phase-dependent effect of individual functions f_k applied to the points x_k, we use the *cumulative perturbation amplification factor* (CPAF) defined by

$$\delta(i, j) = \left| \prod_{k=i}^{j} f'_k(x_k) \right|, \tag{7}$$

as introduced in [20]. By definition, the value $\delta(i, j)$ reflects the total action of the functions f_k, $k = i, \dots, j$ on the phase interval $[i, j]$. Note that this value can be seen as a discrete time analogue to a Floquet multiplier of a limit cycle in a continuous time system. It follows from Eq. (7) that $\delta(0, m-1) = |\lambda(\mathcal{O}_m)|$, so that the stability of $\mathcal{O}_m$ implies $\delta(0, m-1) < 1$. However, on shorter phase intervals $[i, j]$, the CPAF $\delta(i, j)$ may exceed one. In particular, we are interested in the *maximal CPAF* given by

$$\delta_{\max} = \max_{(i,j)} \delta(i, j). \tag{8}$$

As an example, let $I_{\rm exp} = [k_1, k_2 - 1]$ and $I_{\rm contr} = [k_2, k_1 - 1]$ be the expanding and contractive phase intervals of a cycle $\mathcal{O}_m$. By definition, the values $\delta(k_1, j) > 1$ are monotonously increasing for $j \in [k_1, k_2 - 1]$ and reach the maximum by $\delta(k_1, k_2 - 1)$. Similarly, the values $\delta(k_2, j) < 1$ are monotonously decreasing for $j \in [k_2, k_1 - 1]$ and reach the minimum by $\delta(k_2, k_1 - 1)$. Clearly, the stability of $\mathcal{O}_m$ implies

$$\delta(k_2, k_1 - 1) \cdot \delta(k_1, k_2 - 1) < 1 \tag{9}$$

which means that the effect of the expanding functions is compensated by the contractive ones.

For the cycle shown in Fig. 3(a), the phases k_1, k_2 corresponding to the beginning of the expanding and contractive phase intervals,

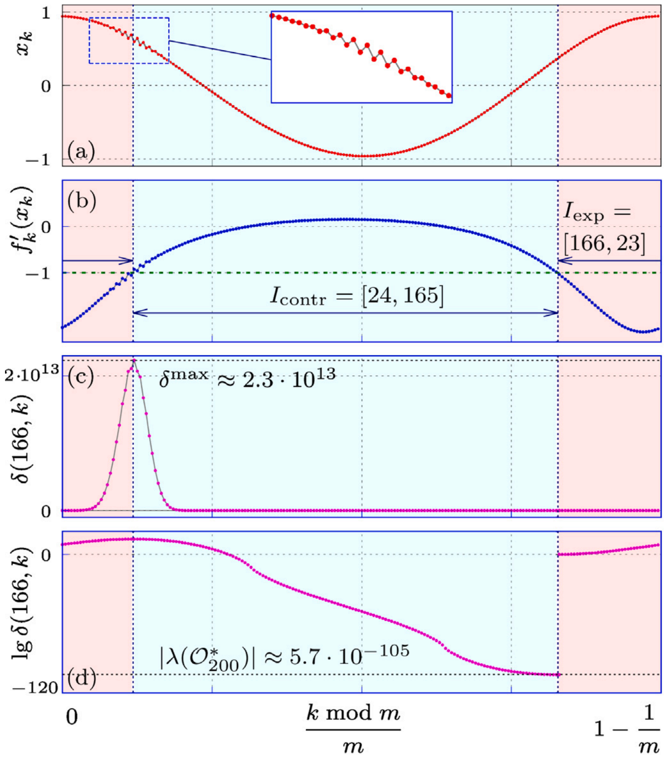

Fig. 4. (a) A bubbling-affected 200-cycle $\mathcal{O}_{200}$ at $\alpha = 10.15$; (b), (c), (d) as in Fig. 3.

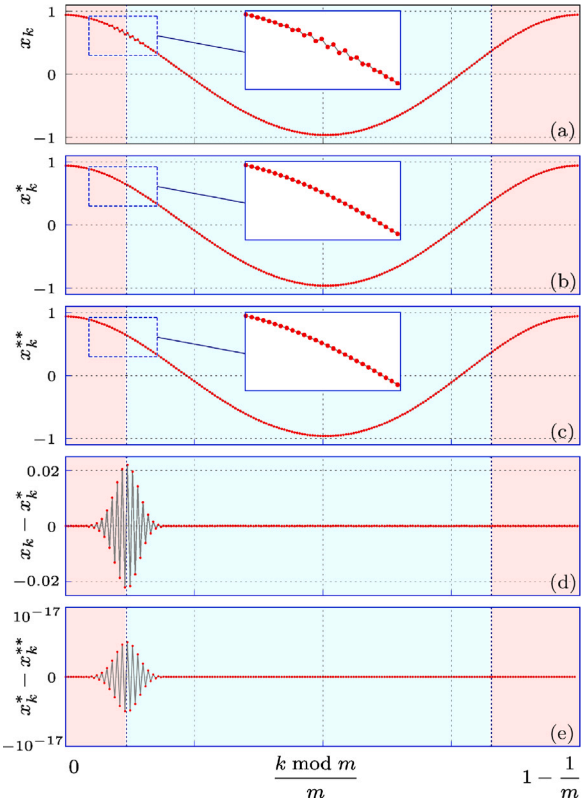

Fig. 5. (a)–(c) Three orbits $\mathcal{O}_{200}$, $\mathcal{O}^*_{200}$, and $\mathcal{O}^{**}_{200}$ of map (6) calculated numerically at the same parameter value $\alpha = 10.15$ with different precision of the numbers used for their calculation. (d) Deviation between $\mathcal{O}_{200}$, $\mathcal{O}^*_{200}$. (d) Deviation between $\mathcal{O}^*_{200}$, $\mathcal{O}^{**}_{200}$.

respectively, are given by $k_1 = 178$, $k_2 = 12$ (see the values $f'_k(x_k)$ in Fig. 3(b)). Thus, the CPAF $\delta(178, j)$ increases throughout the expanding phase interval $I_{\text{exp}} = [178, 11]$ and reaches the maximal value $\delta_{\max} = \delta(178, 11) \approx 435$ at the end of I_{exp} (Fig. 3(c)). Then, the value $\delta(178, j)$ starts to decrease and reaches soon (specifically, at $k = 31$) the values below one. Eventually, at the end of the contractive phase interval (see Fig. 3(d)), the CPAF reaches the value $\delta(178, 177) \approx 5.6 \cdot 10^{-122}$ which is also the multiplier of the considered cycle. Accordingly, the considered cycle is almost super-stable, and a deviation ϵ added to any point of this cycle is reduced by factor higher than 10^{120} after one period of the cycle, i.e., 200 iteration steps. However, a deviation ϵ added to the point at a suitable phase $k \in I_{\text{exp}}$ may also temporarily grow, up to a factor ≈ 435.

Depending on several factors (in particular those discussed below in Section 5), the CPAF may reach much larger values, as illustrated in Fig. 4. In the example presented there, the expanding phase interval is longer than in the example shown in Fig. 3 (approximate by factor 1.7), and the absolute values of the derivatives on this interval are larger (approximate by factor 1.2). However, all these seemingly harmless changes accumulate up, so that in the considered example the maximal value of the CPAF reached at the end of the expanding phase interval is $\delta_{\max} = \delta(166, 23) \approx 2.3 \cdot 10^{13}$. Clearly, a slightest deviation multiplied by such a factor may become visible which explains the phenomenon of noise-induced bubbling reported in [20]. Recall that in physical experiments, noise is unavoidable. Clearly, an initial deviation caused by noise, being amplified by a sufficiently large factor $\delta_{\max}$ may become well-visible. Moreover, it turns out that orbits obtained by numerical simulations using standard double-precision floating point number representation, as for example the orbit shown in Fig. 4, can be seen as being noise-affected as well, in the sense that round-off errors and similar effects act as a kind of initial disturbances. The amplitude of these disturbances is much lower than the noise level in physical experiments, nevertheless, they may also be boosted by a sufficiently large CPAF. It is worth noting that this effect occurs not only in numerical simulations of models similar to map (6), but also when using software tools for so-called equation-free simulations (e.g., PSIM$'$ [23]), as these tools are ultimately affected by the same round-off errors as equation-based simulations.

In the situation described above, it is natural to ask how the exact orbits of map (6) (i.e., theoretically existing orbits calculated with an infinite accuracy) behave at parameter values for which numerically calculated orbits are bubbling-affected. Fig. 5 provides a clear evidence that at the same parameter value as in Fig. 4, the exact orbit of map (6) exhibits no bubbling. In this figure, points of three numerically calculated orbits of map (6) are shown, namely $\mathcal{O}_{200} = \{x_k\}$, $\mathcal{O}^*_{200} = \{x^*_k\}$, $\mathcal{O}^{**}_{200} = \{x^{**}_k\}$, $k = 0..199$. All three orbits are calculated at the same parameter and differ in the precision of the numbers used for the calculation. The first one is calculated using the usual double precision (specifically, numbers with 53 binary digits in the mantissa, which corresponds to about 16 decimal digits). As one can see in Fig. 5(a), this orbit is clearly bubbling-affected. The second and the third orbits are calculated with a higher precision: the numbers used throughout their calculations have 100 and 200 binary digits in the mantissa, respectively, which corresponds to about 30 and 60 decimal digits. In these cases, as shown in Figs. 5(b) and (c), no bubbling is visible.

It is reasonable to assume that the calculations accuracy increases with increasing precision of number representation, so the orbit $\mathcal{O}^*_{200}$ is more accurate than $\mathcal{O}_{200}$, and $\mathcal{O}^{**}_{200}$ is more accurate than $\mathcal{O}^*_{200}$. As one can see in Figs. 5(d) and (e), the difference between the more accurate orbit and the less accurate one reflects the noise-induced bubbling phenomenon: it first increases and then decreases in accordance with the accumulated perturbation amplification factor, reaching the maximal value at the phase corresponding to the end of the expanding phase interval.

4. Archetypal model

So far, we illustrated the recently reported phenomenon of noise-induced bubbling by a specific example given by map (6). To proceed further, let us pose the following question: Which properties of map (6) are relevant for the onset of noise-induced bubbling? As a working hypothesis we assume that neither the specific form of the equations describing the map, nor the resulting waveform of the cycles is important for the onset of noise-induced bubbling but only the presence of expanding and contractive phase intervals $I_{\exp}$ and I_{contr}. To validate this hypothesis, let us define a different – possibly simple – model with this property and examine whether it exhibits a behavior similar to map (6). Once this is confirmed, we can use this model to investigate the bubbling phenomenon (in particular, its dependency on the specific parameters) and expect that the results remain applicable to map (6) as well as to other maps which exhibit this phenomenon (which, of course, necessitates further validation). For this reason, we call the map f defined below an *archetypal model* for the noise induced bubbling phenomenon.

As a first step, let us define the cycle the map f has to exhibit. Let $h(t)$ be a periodic function with the period T defining the overall shape of a desired waveform.[1] Let us consider the samples $x^*_k = h(i/m)$, $i = 0, 1, \dots$, such that $x^*_m = g(T) = g(0) = x^*_0$, and the set of points

$$\mathcal{O}^*_m = \left\{ x^*_k \mid x^*_k = h\left(\frac{k}{m}\right)\right\}_{k=0}^{m-1}. \tag{10}$$

Next, using these points, we can define a set of m linear functions, $f_k(x) = a_k x + b_k$, $k = 0, \dots, m-1$, such that

$$x^*_{k+1} = f_k(x^*_k).$$

By periodicity of h, the points x^*_k, $k = 0, \dots, m-1$, form an m-cycle of the non-autonomous function $f(k, x)$ which is periodic with respect to k and is defined by

$$f(k, \cdot) = f_k, \quad k = 1, \dots, m-1.$$

It follows from the definition of f_k that

$$x^*_{k+1} = a_k x^*_k + b_k,$$

which implies that the offsets b_k are given by

$$b_k = x^*_{k+1} - a_k x^*_k. \tag{11}$$

As for the slopes a_k, they can be chosen arbitrarily, determining the stability of the cycle.

As mentioned above, an initial deviation amplified by expanding functions and leading ultimately to the bubbling phenomenon may be caused by physical or numerical noise. Therefore, we include into the model a stochastic term η added to the actual state variable. For sake of simplicity, we use a stochastic term η following a Gaussian distribution around the mean value $\mu = 0$ and with the standard deviation σ. Note that theoretically setting σ to zero corresponds to switching off the stochastic term η. However, in numerical simulations, this does not exclude noise completely but only reduces it to the level of round-off errors of the double-precision floating point numbers (approximately 10^{-16}).

To sum up, the archetypal model for the investigation of the noise induced bubbling phenomenon is given by

$$\begin{aligned} x_{n+1} &= f(x, k) = a_k x_n + b_k + \eta \\ k &= n \bmod m \end{aligned} \tag{12}$$

where x_n is the state variable at the time instant n, k is its phase, and

- the offsets b_k, $k = 0, \dots, m-1$, are defined by Eq. (11) based of the set of points x^*_k forming the desired waveform h and constituting an m-cycle of map (12);
- the slopes a_k determine the contractive or expanding action of the function on specific functions $f_k \equiv f(\cdot, k)$ in the neighborhood of the points x^*_k,
- the term η reflects the noise present in the underlying physical system.

It is worth emphasizing that the three components of the model listed above are independent from each other and each of them has to be defined separately to match the properties of the specific application under consideration. The points x^*_k have to be chosen according to the shape of the cycle in the modeled applied system, the slopes a_k according to the local stability of these points, and η – or possibly some more sophisticated noise model – according to the actual properties of the physical noise.

To demonstrate a generic nature of map (12) and to illustrate its mode of operation, let us consider two different functions defining the waveforms of the cycles, namely

$$h_1 = x \bmod 1, \tag{13}$$

$$h_2 = \sin(2\pi x). \tag{14}$$

The cycles of map (12) defined by Eq. (10) with these functions are given by

$$\mathcal{O}^*_m = \left\{ x^{\text{saw}}_k \mid x^*_k = \frac{k}{m} \bmod 1 \right\}_{k=0}^{m-1}, \tag{15}$$

$$\mathcal{O}^\star_m = \left\{ x^{\sin}_k \mid x^\star_k = \sin\left(\frac{2\pi}{m} k\right)\right\}_{k=0}^{m-1}, \tag{16}$$

respectively. The latter cycle has a sin-shaped waveform similar to cycles of map (6), while the former one has a sawtooth-shaped waveform.

To illustrate the effect of the CPAF $\delta(i, j)$, let us consider a toy-model where in contrast to map (6), a closed form for $\delta(i, j)$ can be provided. Let the slopes a_k, $k = 0, \dots, m-1$ be defined by

$$a_k = \begin{cases} a^u & \text{if} \quad k < k_0 \\ a^s & \text{if} \quad k \geqslant k_0 \end{cases} \tag{17}$$

with the values a^u, a^s satisfying $a^u < -1$, $-1 < a^s < 0$, and $0 < k_0 < m$. Then, the map is expanding on the phase interval $I_{\exp} = [0, k_0 - 1]$ and contractive on $I_{\text{contr}} = [k_0, m-1]$. Since the slope on both intervals are constant, the CPAFs on these intervals are given by

$$\begin{aligned} \delta(0, k_0 - 1) &= |(a^u)|^{k_0}, \\ \delta(k_0, m-1) &= |(a^s)|^{m-k_0}. \end{aligned} \tag{18}$$

Accordingly, the multiplier of the m-cycle $\mathcal{O}^*_m$ is given by $\lambda(\mathcal{O}^*_m) = (a^u)^{k_0}(a^s)^{m-k_0}$ and the cycle is stable as long as $|a^s| < |a^u|^{-k_0/(m-k_0)}$. By construction, the maximal CPAF is given by $\delta_{\max} = \delta(0, k_0 - 1)$.

An example of a cycle $\mathcal{O}^*_m$ defined by Eq. (15) with the slopes a_k given by Eq. (17) is shown in Fig. 6. Here, to improve the visibility, a very small value $m = 7$ is used. As one can immediately see, with $k_0 = 3$ the first three functions $f_0, \dots, f_2$ are expanding, and the following four $f_3, \dots, f_6$ are contractive, so that in the presented example the contractive and expanding intervals are given by $I_{\exp} = [0, 2]$ and $I_{\text{contr}} = [3, 6]$, respectively.

An example of a time series of map (12) with the same definitions (15), (17), and a higher value $m = 400$ is shown in Fig. 7. The distortion of the signal close to the phase $k = 100$ is clearly visible. Note

---

[1] To avoid possible misunderstandings, the term "overall shape" deserves a comment. By construction, exact waveforms of signals in a switching system such as for example the inverter described in Section 2 are given by piecewise smooth curves with break points at every switching event. The same applies to their continuous-time models. However, a discrete-time model of such a system given by a stroboscopic mapping at the switchings associated with clock events, as for instance map (6), does not reflect the dynamics between these events. Therefore, the discrete-time waveform of such a model can be seen as belonging to a (possibly smooth) curve (a kind of envelope) which reflects the overall shape of signals in continuous time neglecting their small-amplitude oscillations between clock events. For example, the overall shape of waveforms in map (6) is approximate sinusoidal.

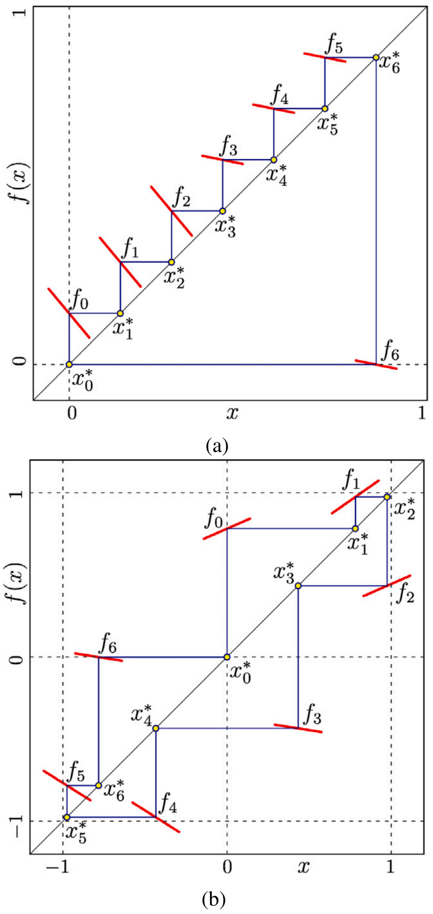

(a)

(b)

Fig. 6. Examples of cycles $\mathcal{O}_7^*$ and $\mathcal{O}_7^*$ corresponding to (a) saw-tooth (see Eq. (15)) and (b) sinus-shaped (Eq. (16)) waveforms of the signals. To improve the visibility, the functions f_k, $k = 0, \ldots, 6$ are shown in the neighborhoods of the points x_k they are acting on. The slopes a_k of the functions f_k are defined by Eqs. (17) and (19), respectively. Parameters: $m = 7$, (a) $k_0 = 3$, $a^u = -1.2$, $a^s = -0.5$; (b) $c_0 = 0$, $c_1 = 0.7$.

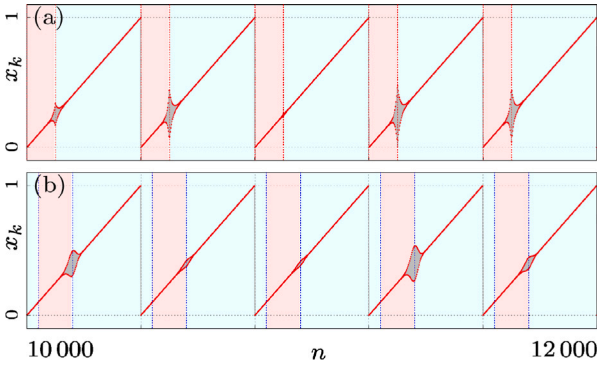

Fig. 7. Time series of map (12) with the saw-tooth shaped m-cycle, $m = 400$, defined by Eq. (15). The slopes a_k are given by (a) Eq. (17) with $a^u = -1.17$, $a^s = -0.9$, $k_0 = 100$, $\sigma = 10^{-8}$; and (b) Eq. (19) with $c_0 = -0.7$, $c_1 = -0.5$, $\sigma = 10^{-8}$.

that the maximal distortion amplitude in each period differs, which is not surprising as it results from the amplification of the random term η.

An advantage of the archetypal model (12) is that the exact (unperturbed) cycle $\mathcal{O}_m^*$ is known and thus, the deviation of the actual cycle $\mathcal{O}_m$ obtained numerically can easily be determined. As an illustration, Fig. 8 shows the deviation of the perturbation-affected cycle $\mathcal{O}_m$ corresponding to the numerically calculated time series presented in Fig. 7 from the exact cycle $\mathcal{O}_m^*$ given by Eq. (15). The stability of the exact cycle can easily be validated: $|\lambda(\mathcal{O}_{400}^*)| = (a^u)^{100}(a^s)^{300} \approx 1.2 \cdot 10^{-7} \ll 1$. However, the CPAFs on the expanding phase interval is quite large: by Eq. (18), we obtain $\delta(0, 99) \approx 6.6 \cdot 10^6$. Therefore, in Fig. 8 we observe first a well-visible exponential growth of the deviation $|x_k - x_k^*|$ on the interval I_{exp}, and then its exponential decay on the interval I_{contr}. It is also clearly visible that the phase k_0 corresponding to the end of the expanding phase interval and the begin of the contractive one, is also the phase associated with the maximal amplitude of the deviation $|x_k - x_k^*|$.

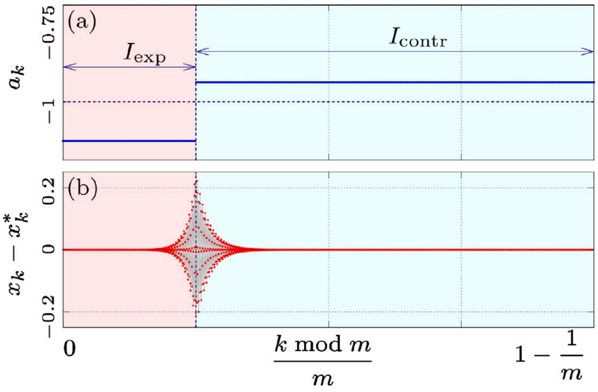

Fig. 8. (a) Slopes a_k defined by Eq. (17). (b) Distance between the exact cycle $\mathcal{O}_m^*$ given by Eq. (15) and the cycle $\mathcal{O}_m$ shown in Fig. 7(a). The phase of the points of the cycle is shown normalized to the interval $[0, 1)$. Parameters as in Fig. 7(a).

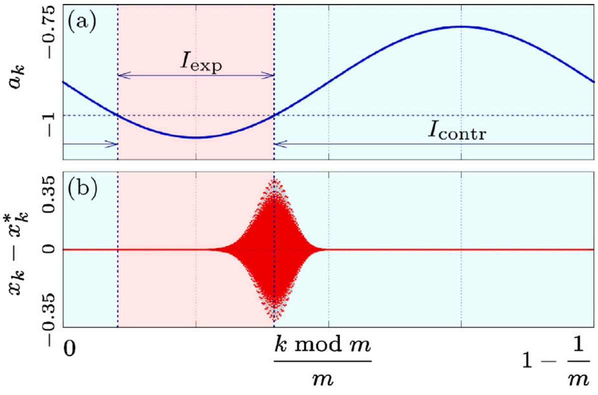

Fig. 9. (a) Slopes a_k defined by Eq. (19). (b) Resulting distance between the exact cycle $\mathcal{O}_m^*$ given by Eq. (15) and the cycle $\mathcal{O}_m$ calculated numerically. Parameters: $m = 400$, $c_0 = -0.7$, $c_1 = -0.5$, $\sigma = 10^{-8}$.

In the previous example, the slopes a_k are constant in the expanding/contractive phase intervals and change discontinuously. This provides us with analytic expressions for the CPAFs, but does not match applications showing the bubbling phenomenon where the corresponding values $f_k'(x_k)$ change gradually, as for example in map (6). Therefore, let us consider the next example where the slopes a_k, $k = 0, \ldots, m-1$, are defined by a smooth function taking the values both above and below -1:

$$a_k = c_0 + c_1 \sin\left(\frac{2\pi k}{m}\right). \tag{19}$$

An example of the action of map (12) with the exact cycle $\mathcal{O}_m^*$ following – as before – the sawtooth function but the slopes a_k defined by Eq. (19) is shown in Fig. 7(b). Here, one can already recognize the shape of the distortion of the cycle similar to the one observed in map (6). This shape is even more clear visible in Fig. 9 showing the difference between the actual time series and the exact cycle $\mathcal{O}_m^*$. In the presented example, the expanding interval of $\mathcal{O}_m^*$ is given by $I_{\text{exp}} = [41, 159]$. Straight forward computation shows that the multiplier of the exact cycle is given by $\lambda(\mathcal{O}_m^*) \approx 6.2 \cdot 10^{-91}$, while the CPAFs on the expanding

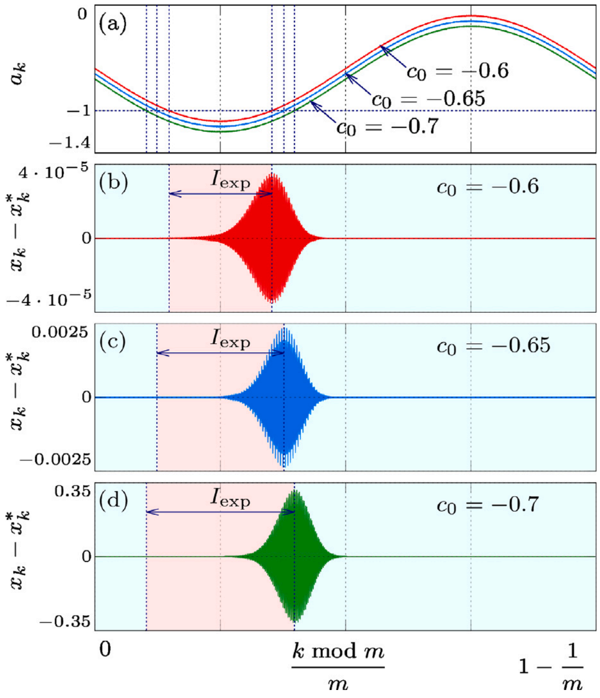

Fig. 10. (a) Slopes a_k defined by Eq. (19) for three different values of c_0. (b), (c), (d) Resulting distance between the exact cycle $\mathcal{O}_m^*$ and the cycle $\mathcal{O}_m$ calculated numerically. Parameters: $m = 400$, $c_1 = -0.5$, (b) $c_0 = -0.6$, (c) $c_0 = -0.65$, (d) $c_0 = -0.7$.

phase interval is $\delta(41, 159) \approx 1.8 \cdot 10^6$. The maximal bubbling amplitude is reached at the beginning of the contractive phase interval, i.e., for $k = 160$. By contrast to the previous example, the envelopes of the deviation $x_k - x_k^*$ at this point have zero derivative. This is easily explained, as the coefficients a_k considered as a function depending on k cross the -1 threshold, and therefore close to this value the functions f_k have only a very weak expanding or contractive effect.

5. Influence of parameters

Let us now examine how the effect of the expanding phase interval changes under variation of the parameters determining the slopes a_k. In particular, we are interested in the changes of $\delta_{\max}$ given by Eq. (7).

As already mentioned, for the toy-model, i.e., in the case that the slopes are given by Eq. (17), this value is given by $\delta_{\max} = |(a^u)^{k_0}(a^s)^{m-k_0}|$, as follows directly from Eq. (18). Then

1. With increasing length of the expanding phase interval I_{exp}, the CPAF $\delta_{\max}$ grows exponentially. This reinforces the bubbling effect.
2. With increasing absolute value of the slopes a^u, the CPAF exhibits polynomial growth. This reinforces the bubbling effect as well, but not as strong as the increase of the length of the expanding phase interval.

The occurrence of bubbling in real-world application is usually a combination of points (1) and (2) introduced by the variation of parameter as illustrated in [19]. Note also that increasing or decreasing values of the slopes a^s do not influence the strength of bubbling but only the duration until bubbling vanishes in the contractive phase interval.

For the case that the slopes a_k are given by Eq. (19), such analytical results are less immediate. Fig. 10 shows the deviation of the disturbance-affected cycle $\mathcal{O}_m$ calculated numerically from the exact cycle $\mathcal{O}_m^*$ under variation of the value c_0. As one can see in Fig. 10(a), for increasing absolute value of c_0, the coefficients a_k move in negative direction and additionally, the length of the expanding phase intervals increases. Specifically, for $c_0 = -0.6$, $c_0 = -0.65$, and $c_0 = -0.7$ we obtain $I_{\text{exp}} = [60, 140]$, $I_{\text{exp}} = [50, 150]$, and $I_{\text{exp}} = [41, 159]$, respectively. As a result, the amplitude of the distortion grows rapidly, from $\sim 10^{-5}$ for $c_0 = -0.6$ to $\sim 10^{-1}$ for $c_0 = -0.7$. This is easily explained by the corresponding maximal cumulative perturbation amplification factors: straightforwardly, we obtain $\delta_{\max} = \delta(60, 140) \approx 1.8 \cdot 10^2$ for $c_0 = 0.6$, $\delta_{\max} = \delta(50, 150) \approx 1.3 \cdot 10^5$ for $c_0 = 0.65$, and $\delta_{\max} = \delta(41, 159) \approx 1.8 \cdot 10^6$ for $c_0 = 0.7$. Note that in practical applications, the distortion in the former case can easily be overlooked, while in the latter case it can be well-visible. Nevertheless, it is worth emphasizing that the existence of an expanding phase interval implies that the distortion exists, and the waveform is distorted starting from the beginning of this interval, even if it is not immediately noticeable there.

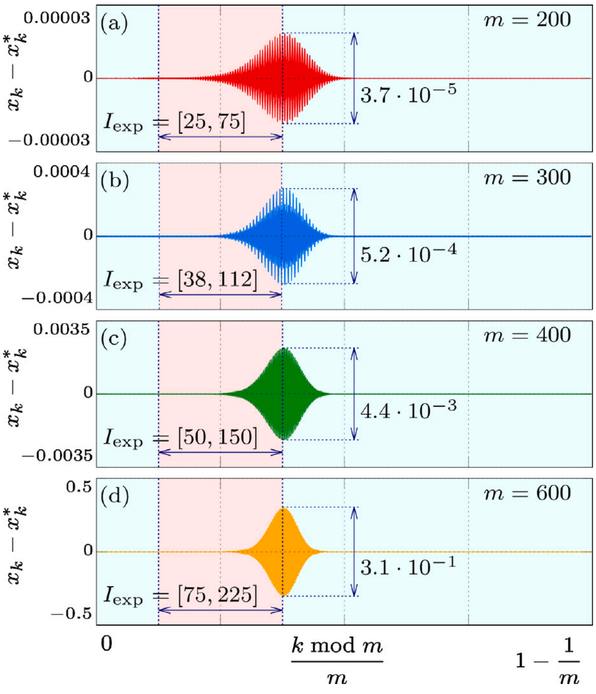

Fig. 11. Deviation between $\mathcal{O}_m$ and $\mathcal{O}_m^*$ for increasing frequency modulation ratio m. Slopes a_k are defined by Eq. (19). $c_0 = -0.65$, $c_1 = -0.5$, $\sigma = 10^{-8}$.

One more effect visible in Fig. 10 is the displacement of the phase interval where bubbling is well-observable with increasing length of I_{exp}. This is not surprising, since these intervals are centered around the right end points of I_{exp}.

As a next step, let us examine how the parameter m corresponding to the frequency modulation ratio in power electronics applications influences the intensity of bubbling. It is worth noting that commonly, in practical applications increasing the frequency modulation ratio improves the quality of the signals, decreasing the undesired high frequency oscillations. However, this is not the case for such oscillations caused by the bubbling phenomenon. Indeed, the amplitude of the oscillations caused by this effect is determined by the number of points belonging to the expanding phase interval. If the parameter m is increased while the other parameters are kept unchanged, the number of expanding points is increased as well, and accordingly, the bubbling amplitude grows. This is illustrated in Fig. 11. As indicated in this figure, under variation of m from 200 to 600, this amplitude increases from $\sim 10^{-5}$ to $\sim 10^{-1}$. This is not surprising, since for increasing m the length of the corresponding expanding intervals grows, and although the values of the slopes a_k do not change (since the coefficients c_0, c_1 are fixed), the resulting maximal CPAFs grow from $\delta_{\max} = \delta(25, 75) \approx 1.1 \cdot 10^3$ in Fig. 11(a) to $\delta_{\max} = \delta(38, 112) \approx 1.2 \cdot 10^4$ in Fig. 11(b), $\delta_{\max} = \delta(50, 150) \approx 1.3 \cdot 10^5$ in Fig. 11(c), and $\delta_{\max} = \delta(75, 225) \approx 1.5 \cdot 10^6$ in Fig. 11(d).

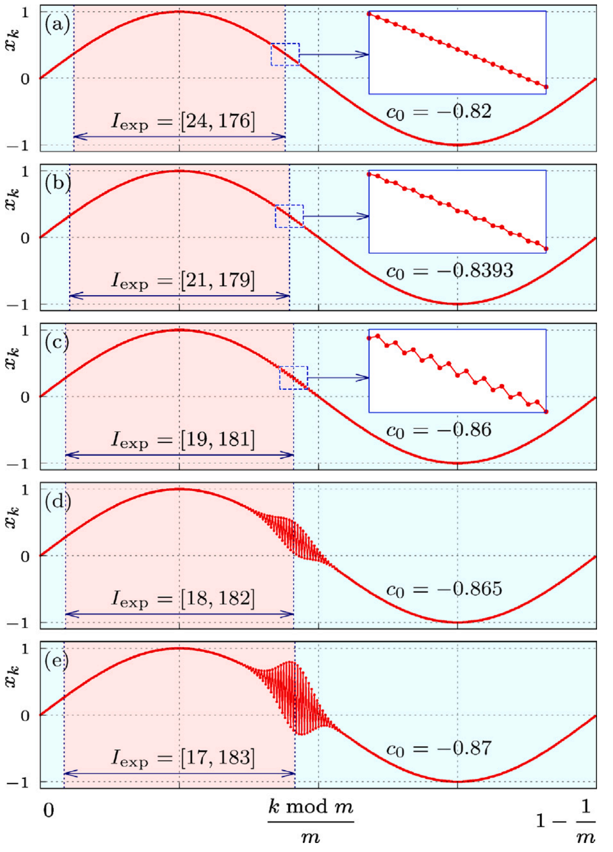

Fig. 12. Gradual onset of bubbling in map (12) caused by increasing cumulative perturbation amplification factor under variation of c_0 in the definition of the slopes a_k given by Eq. (19). (a) no visible distortion; (b) simmering effect (precursor of bubbling, visible in the inset); (c) weak bubbling (visible in the inset); (d), (e) well-developed bubbling. Parameter values: $m = 400$, c_0 varied from -0.82 to -0.87 as indicated, $c_1 = -0.5$, $\sigma = 0$.

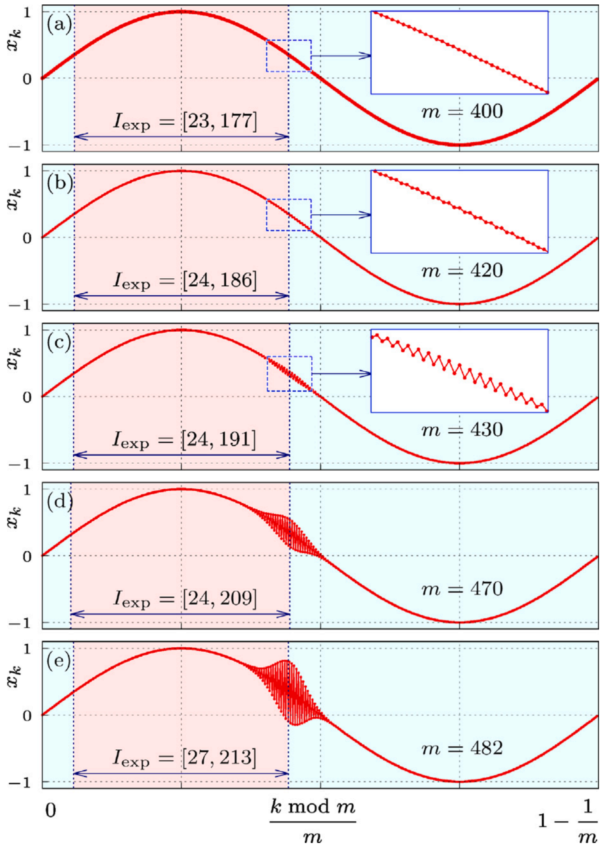

Fig. 13. Gradual onset of bubbling in map (12) caused by increasing CPAF under variation of m. (a) no visible distortion at $m = 400$; (b) simmering effect at $m = 420$; (c), (d) weak bubbling at $m = 450$ and $m = 500$; (e) well-developed bubbling at $m = 540$. Parameter values: $c_0 = -0.83$ $c_1 = -0.5$, $\sigma = 0$.

As a side remark we note that despite its negative effect on the intensity of bubbling, increasing the frequency modulation ratio m may have other positive effects (which is in-line with the common practice in power electronic circuits). For example, it may "increase the stability" of cycles. To illustrate that, consider again map (12) with the slopes a_k defined by Eq. (17). As already mentioned, in this case a stable m-cycle has the multiplier $\lambda(\mathcal{O}^*_m) = (a^u)^{k_0}(a^s)^{m-k_0}$ with $|\lambda(\mathcal{O}^*_m| < 1$. Increasing m by factor two, we obtain a $2m$-cycle with the multiplier

$$\lambda(\mathcal{O}^*_{2m}) = (a^u)^{2k_0}(a^s)^{2(m-k_0)} = (\lambda(\mathcal{O}^*_m))^2, \tag{20}$$

which implies $|\lambda(\mathcal{O}^*_{2m})| < |\lambda(\mathcal{O}^*_m)| < 1$.

So far we considered the deviation of the disturbance-affected cycles $\mathcal{O}_m$ from the corresponding exact values $\mathcal{O}^*_m$. For completeness, let us now illustrate how the expanding phase intervals affect the waveforms of cycles similar to those of map (6). To this end, let us consider the cycles $\mathcal{O}^\star_m$ with sinus-shaped waveforms defined by Eq. (16) using the function h_2 (see Eq. (14)). As for the slopes a_k, we keep them defined by Eq. (19). An example of such a cycle in shown in Fig. 6(b).

Fig. 12 illustrates how the increasing amplitude of the distortion amplified by expanding functions becomes visible in the waveform of the cycle $\mathcal{O}_m$, reproducing the usual onset of bubbling. For simplicity, in the presented example we switch off the additive noise by setting $\sigma = 0$, such that the initial deviation amplified by expanding functions in numerical experiments is related solely to numerical (round-off, etc.) errors. As illustrated in Fig. 12(a), at $c_0 = -0.82$ the map has already an extended expanding interval $I_{\exp}$, and the CPAF on this interval has already a considerable value $\delta(24, 176) \approx 2.18 \cdot 10^{12}$. Still, this amplification is not sufficient to cause a recognizable distortion of the waveform.

Then, with increasing absolute value of c_0, the CPAF on the expanding phase interval increases and the oscillations become more and more visible. First, we observe the onset of simmering (see Fig. 12(b) with $\delta_{\max} = \delta(21, 179) \approx 2.63 \cdot 10^{13}$). Here, specific points of the observed cycle do not constitute local minima and maxima of the waveform. Nevertheless, close to the end of $I_{\exp}$, the distortion can already be noticed (see the inset in Fig. 12(b)).

As the absolute value of c_0 and hence the CPAF is further increased, the typical onset of bubbling with a gradually increasing amplitude can be observed (see Figs. 12(c), (d), (e) with $\delta_{\max} = \delta(19, 181) \approx 4.08 \cdot 10^{14}$, $\delta_{\max} = \delta(18, 182) \approx 8.0 \cdot 10^{14}$, $\delta_{\max} = \delta(17, 183) \approx 1.57 \cdot 10^{15}$, respectively). For higher values of $|c_0|$, the distortion is even higher, however, here the dynamics of the archetypal model does not correspond to the dynamics of map (6), since in simulations of the latter model the maximal distortion amplitude is restricted by the action of the branches $g^{\mathcal{L}}$, $g^{\mathcal{R}}$ corresponding to the saturation regime. This effect is not modeled by map (12) but can easily been restored, e.g., by the piecewise linear model suggested in [24].

A similar effect obtained under variation of m is illustrated in Fig. 13. The results here do not differ from the ones obtained for the sawtooth-shaped cycles defined by Eq. (15) and discussed above. As before, for increasing values of m we observe increasing distortion of the waveform manifesting itself first as simmering (Fig. 13(b)) and then as bubbling (Fig. 13(c)–(e)).

It is worth noting that the existence of an expanding phase interval is a necessary but not a sufficient condition for the onset of the noise-induced bubbling. Indeed, the oscillation of a perturbed solution

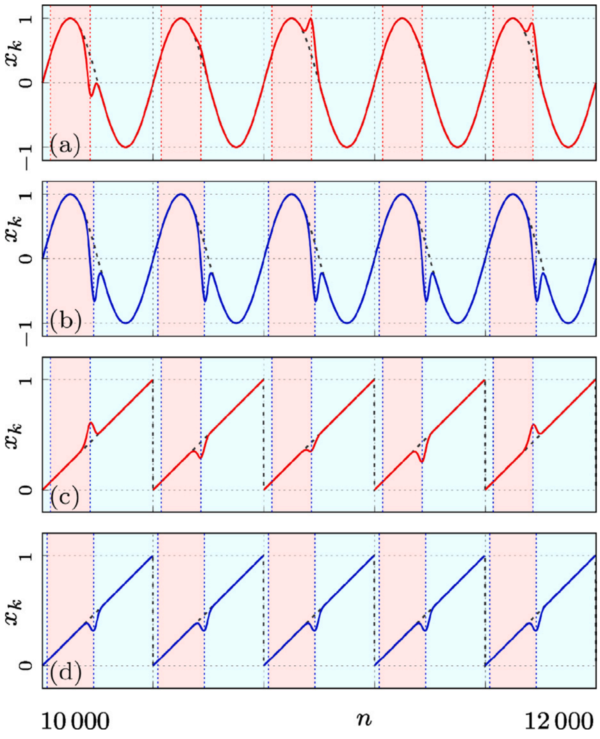

Fig. 14. Effect caused by an expanding phase interval with $a_k > 1$ (a), (c) in presence of noise; (b), (d) in absence of noise. In (a), (b), the cycles with sinus-shaped waveforms (see Eq. (16)), in (c), (d) cycles with saw-tooth-shaped waveforms (Eq. (15)) are shown. The slopes a_k are defined by Eq. (19), contracting and expanding phase intervals are indicated by colors. Dashed curves show the location of exact cycles. Parameters: $m = 400$, $c_1 = 0.5$, (a), (c) $c_0 = 0.79$, $\sigma = 10^{-12}$, (b), (d) $c_0 = 0.88$, $\sigma = 0$.

around the exact one requires the slopes a_k in map (12) (or, in general, the derivatives f_k) to be negative. Accordingly, the condition $|a_k| < 1$ defining the expanding phase intervals discussed above can also be written as $a_k < -1$. The question may arise about the effect of expanding phase intervals associated with the condition $a_k > +1$. In such a case, an initial distortion becomes amplified as well, but it accumulate unidirectionally. Similar to bubbling, it reaches the maximal amplitude and the end of the expanding phase interval and eventually becomes damped out by contractive functions. Examples of this effect in map (12) are presented in Fig. 14. Here, as one can see in Figs. 14(a), (c), an initial perturbation caused by noise (modeled in map (12) by the random term η) may lead to a different distortion in each period of the exact cycle. Without this term (see Figs. 14(b), (d)), a distortion caused by numerical errors (such as round-off errors) may lead to the same distortion in each period of the exact cycle.

6. Experimental confirmation

To verify the theoretical findings and the numerical simulations, an experimental prototype of the considered H-bridge inverter was constructed following the schematic circuit diagram shown in Fig. 1. Note that the setup was designed to support, among other experiments, an investigation of the noise influence on the circuit's functioning. For this purpose, the noise signal generator GwInstek MFG-2260M was used, allowing a variable intensity noise signal.

6.1. Experimental setup

Fig. 15 the shows hardware realization of the power (upper part) and control (lower part) circuits separately. The four switches $S_1 - S_4$ have been implemented using two legs built up by MOSFET STW45NM50 with two drivers IRS21834. Two control signals u_1 and u_2 are used by these drivers to generate gate signals ($G_1 - G_4$) of the switches after adding dead time between them for shoot-through prevention. Using resistor, the pin 4 (DT) of the driver IC can choose suitable dead time. By connecting pin 4 to the logic ground pin 3, typical dead time 0.4 μs is obtained. Two identical toroidal inductance coils from Coilcraft were used for the load inductance L. Each coil has a nominal inductance of 560 μH, resulting in a total load inductance L of 1.12 mH. These inductors were connected on both sides of the load resistance R. The inverter was fed by an input voltage $E_0 = 15.8$ V and loaded by one resistance R of 10 Ω. The load resistance voltage $V_{\text{out}} = R \cdot i$ was sensed by an amplifier AD629 with a gain $\beta = 1/5$.

To generate the switching signals for the inverter, firstly, a noise signal V_N is added to the sensed and scaled output voltage using operational amplifier TL084 and the resulting signal $\beta V_{\text{out}} + \text{V}_N$ is subtracted from the sinusoidal reference voltage $V_{\text{ref}}(t) = V_m \sin(2\pi \cdot f_{\text{ref}} t)$ to create the error signal at the output of the corrector amplifier DA_2 (see Fig. 1). The reference signal $V_{\text{ref}}(t)$ was provided by the signal generator GwInstek MFG-2260M. In all the experiments, the amplitude of the reference signal was $V_m = 2.0$ V and its frequency f_{ref} was varied. Secondly, the output signal of DA_2 is compared by the comparator DA_1 (Fig. 1) with a periodic ramp signal $V_{\text{ramp}}(t)$ of upper threshold 0.25 V, lower threshold 0.0 V and the frequency of 50 kHz. The comparator DA_1 was implemented by the IC LM319. The ramp signal $V_{\text{ramp}}(t)$ varies in synchrony with the clock signal V_{clock}. The signal V_{clock} is fed to the S-input of the flip-flop DD_1 which set its state of the logical unit. The R-S flip-flop generates the switching signals, in accordance with the sinusoidal pulse-width modulation technique, to the switches $S_1 - S_4$. For implementation of R-S flip-flop, IC device CD4013 was used.

The experimental waveforms shown below have been captured using the Mixed Domain Oscilloscope model Tektronix MDO3014. The output voltage on the load resistor R was measured and displayed in oscilloscope using voltage differential probe TESTEC TT-SI 9001. The complete experimental setup is depicted in Fig. 16.

6.2. Experimental results

The key message of the theory presented above using the archetypal model (12) is that bubbling is caused by the amplification of noise. In real-world applications, noise is unavoidable, and its increasing level may cause the onset of bubbling. To confirm this, let us consider the behavior of the experimental setup for increasing noise level which is achieved, by construction, by increasing the voltage V_N. The results of this experiment are shown in Fig. 17. As one can see in Figs. 17(a) and (b), as the additional noise is switched off, i.e., for $V_N = 0$, no bubbling occurs at the considered values of the other parameters. Then, switching the noise on ($V_N = 20$ mV), we observe the onset of bubbling as illustrated in Figs. 17(c), (d). Note that location of the bubbling-affected phase interval (the beginning of the down-slope of the signal) is as predicted, i.e., it surrounds the end of the expanding phase interval in map (6) as reported in [19]. As the noise level is increased further, the intensity of bubbling increases as well. This is illustrated in Figs. 17(e), (f) and 17(c), (d), showing the results for $V_N = 40$ mV and $V_N = 60$ mV, respectively. It is also well-visible that the amplitude of bubbling does not change much for different noise levels. This result is as predicted as well, because in the real system this amplitude is restricted by the saturation which is present in the control scheme of the circuit and is modeled in map (6) by the branches $g^{\mathcal{L}}$, $g^{\mathcal{R}}$ but not in map (12). Therefore, the bubbling amplitude is beyond the archetypal model given by map (12), although, if necessary, the model can be extended to reflect it as well. In the present form, the amplitude of bubbling-related oscillations in map (12) is characterized by smooth minima and maxima of the envelopes as, e.g., in Figs. 12 and 13, while in the experimental waveforms (Figs. 17 and 18), these minima and maxima are cut off and the amplitude remains – over bubbling-affected phase intervals – close to the level determined by the saturation.

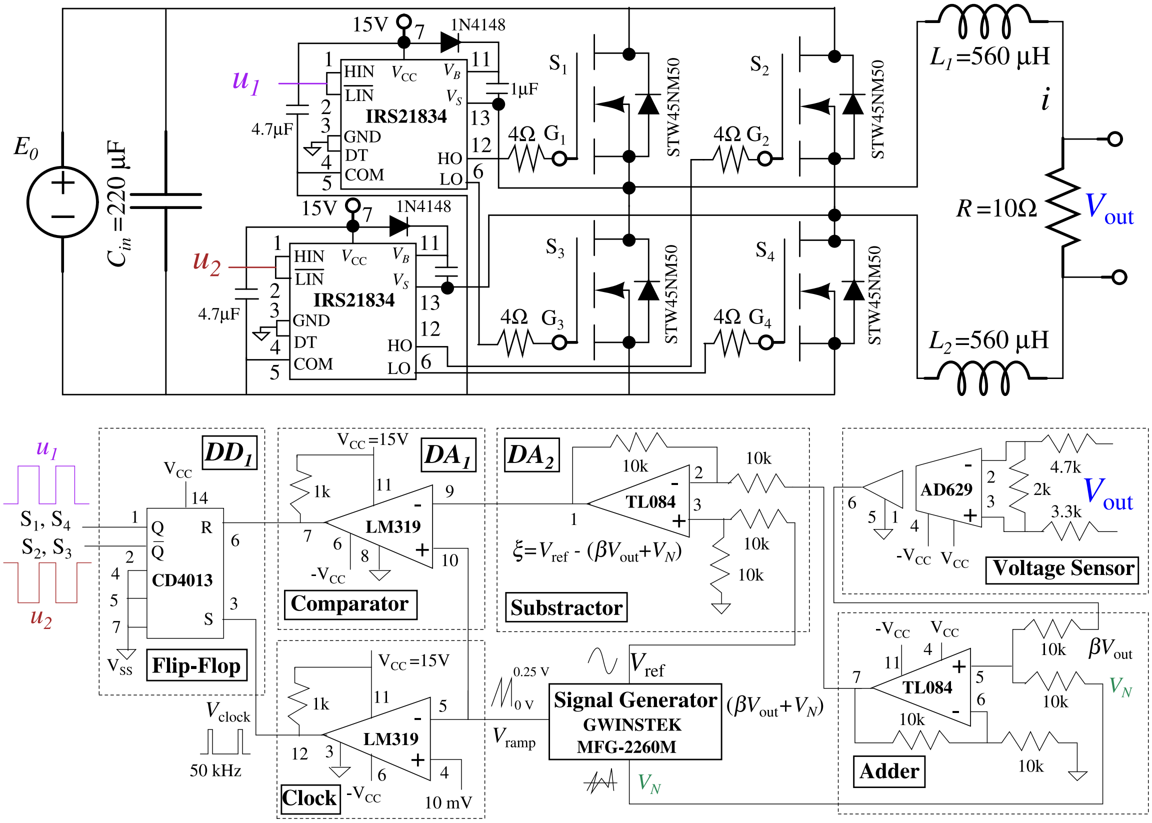

Fig. 15. Schematic diagram of the power and control circuits with component type and values for the experimental setup.

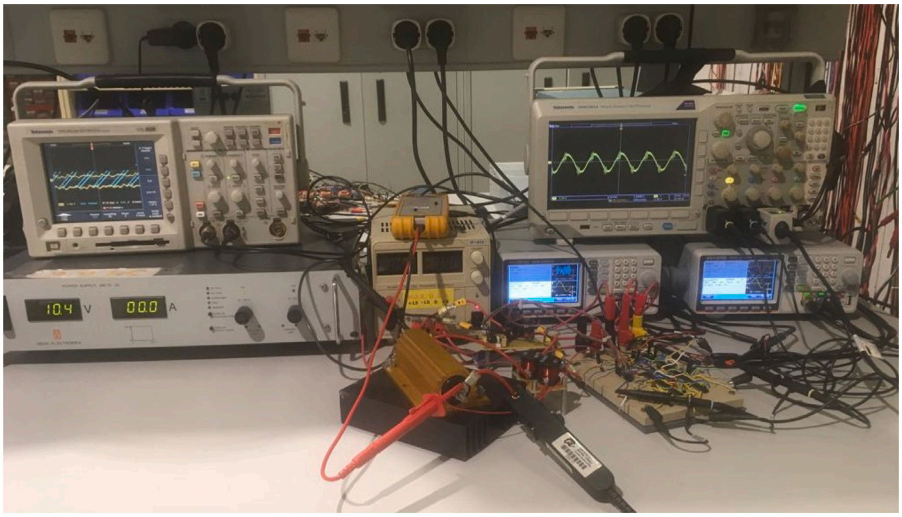

Fig. 16. Experimental setup with power and control circuits, oscilloscope, DC voltage source and function generator.

It is worth noting that the bubbling-affected phase intervals in Figs. 17(d), (f), (h) are interrupted by short phase intervals with no visible bubbling. This can be explained by taking into consideration the stochastic nature of noise. Indeed, subjected to random distortion, the signal may accidentally enter a non-bubbling state space interval. Then, the action of expanding functions, combined again with noise, forces the signal to eventually lead these intervals, returning to the bubbling state. However, for a short time before this occurs, the described effect causes bubbling to disappear in some phase intervals. Note that the length of these intervals decreases with increasing noise level (cf. Figs. 17(d), (f), (h)). Since the other parameters were fixed and hence the expanding functions in the respective phase intervals were the same, we conclude that noise is essential in causing the orbits to leave the non-bubbling intervals in the state space.

In practical settings, one is more interested in how the dynamics is influenced by parameters other than the noise level. As an example, let us consider the behavior of the experimental setup for increasing values of the frequency modulation ratio m. In general, it is commonly believed that higher values of m lead to a better quality of the output signals, lower ripple oscillations, and other positive effects. However, as predicted by the archetypal model (12), it may also have a negative effect, namely that increasing the value of the frequency modulation ratio may cause bubbling to occur.

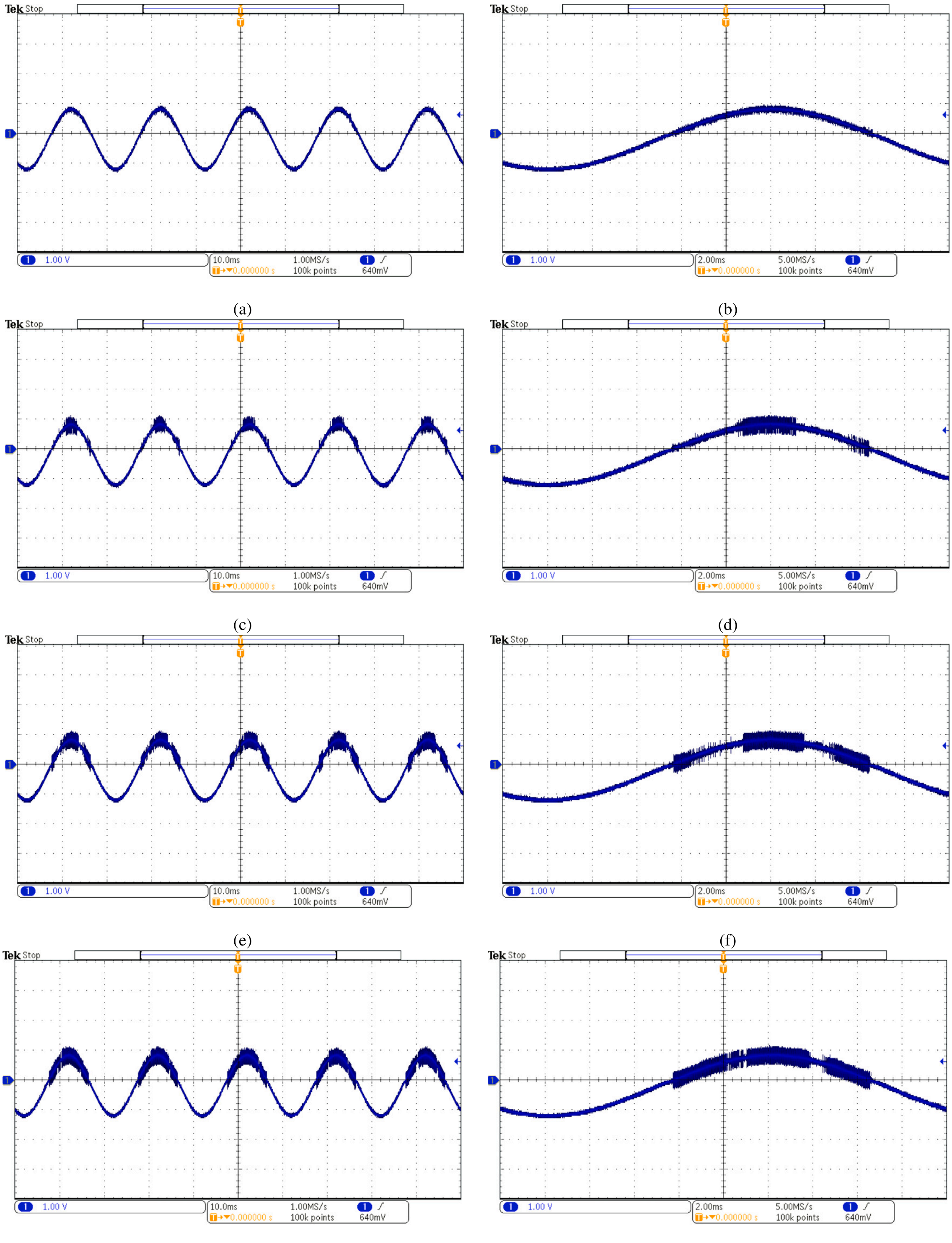

(a) (b) (c) (d) (e) (f) (g) (h)

Fig. 17. Output voltage waveform (a), (b) in absence of noise and (c)–(h) in presence of noise of increasing amplitude. (a), (b) $V_N = 0$ mV, (c), (d) $V_N = 20$ mV, (e), (f) $V_N = 40$ mV, (c), (d) $V_N = 60$ mV. The left column shows five cycles of the signals, the right column shows one cycle magnified. 1/10 attenuation probe was used to measure the output voltage and to display it in the oscilloscope screen.

The experimental results are illustrated in Fig. 18. Here, the increasing values of $m = f_{\mathrm{sw}}/f_{\mathrm{ref}}$ are achieved by fixing the switching frequency f_{sw} and varying frequency f_{ref} of the reference signal while the additional noise is switched off ($V_N = 0$). For a low value of the frequency modulation ratio $m = 167$ (see Fig. 18(a)), the resulting signal is bubbling-free. As it is increased to $m = 400$, we observe a small bubbling-affected phase interval on the down-slope of the signal (Fig. 18(b)). Eventually, as m is increased further (see the cases of $m = 500$ and $m = 1000$ in Fig. 18(c) and (d), respectively), the bubbling-affected interval grows in size, as predicted.

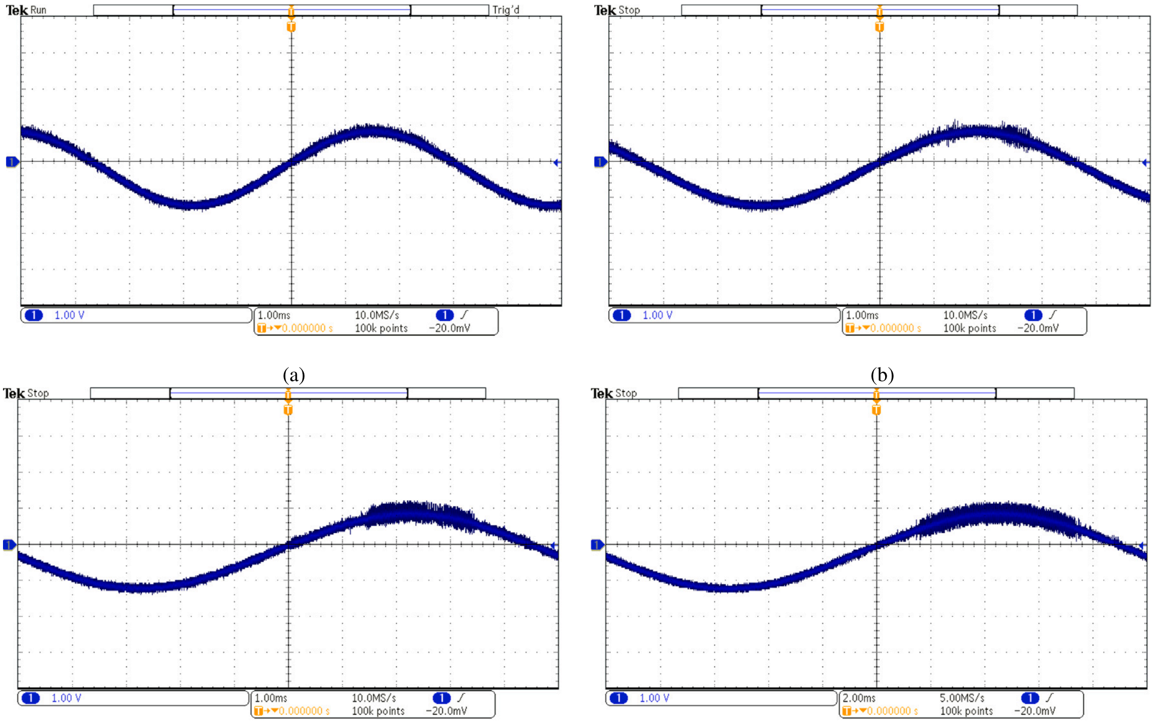

(a) (b)

(c) (d)

Fig. 18. Output voltage waveform under variation of the frequency modulation ratio $m = f_{sw}/f_{ref}$. (a) $f_{ref} = 150$ Hz ($m = 167$), (b) $f_{ref} = 125$ Hz ($m = 400$), (c) $f_{ref} = 100$ Hz ($m = 500$), (d) $f_{ref} = 50$ Hz ($m = 1000$). 1/10 attenuation probe was used to measure the output voltage and to display it in the oscilloscope screen.

The question arises whether the presented results can lead to some practical design advice to avoid undesired oscillations. Recall that, in practice, the switching frequency is much higher than the AC reference frequency, and hence, m is a large number. Therefore, it is a common practice to apply the so-called quasi-static approximation for which allows performing the linear stability analysis in discrete time [25]. This approach will predict that the system will be bubbling-free if the amplitude of the ramp signal V_o is larger than a critical value $V_{o,crit}$ given by the following expression

$$V_{o,crit} = \frac{aR\alpha^2 V_{ref}}{4L(1+\alpha)}.$$

However, the quasi-static approximation does not consider noise and hence, the above condition does not prevent noise-induced bubbling.

This drawback can be avoided using the archetypal model proposed in the present work. Since this model is formulated in terms of generalized parameters a_k, b_k, it does not immediately provide a condition for bubbling-free behavior in terms of the parameters of the original model. Rather, it provides general statements such as that increasing noise level may provoke bubbling and that increasing the frequency modulation ratio m may have the same effect. Moreover, it suggests that numerical computation of CPAF which can easily be performed for a given circuit design by evaluating the derivatives determining the coefficients a_k of the archetypal model provides insight into the extent to which the circuit is affected by the noise-induced bubbling phenomenon. Indeed, comparing between several circuit designs, one should prefer the design that leads – for a given set of parameters – to a smaller value of CPAF.

7. Conclusions

In the present work, we investigated the mechanism leading to the onset of noise-induced bubbling. This mechanism, first reported in [19, 20], involves a cumulative amplification of disturbances, resulting in well-visible high-frequency oscillations of signals' waveform within a restricted phase interval. As mentioned in the cited works, in physical experiments the disturbances leading eventually to the offset of bubbling are related to noise, while in simulations (both equations-based and equation-free ones) it can be attributed to the round-off errors from representing real numbers in computers. In [20], we confirmed this theory using numerical experiments. In the present work, we also provided its experimental confirmation reporting for the first time the onset of bubbling at increasing noise level.

As a motivating example, we considered a model of an H-bridge DC-AC inverter with inductor current feedback and fixed frequency PWM of type 2 already discussed in [19,20]. We identified the properties of this model that are relevant for the bubbling phenomenon, and developed a minimal (archetypal) model that possesses these properties. The model is kept as generic as possible and can be instantiated to reproduce bubbling in signals of arbitrary shapes and with arbitrary stability properties.

For each specific instance, the archetypal model shows how the distortions (of any nature) are amplified starting from the beginning of the expanding phase interval and are eventually damped out in the contractive one. Note that as long as the amplitude of these distortions is much smaller than the amplitude of the overall signal, the resulting high-frequency oscillations may not become immediately visible but rather at a later phase. In the archetypal model, the amplitude of the high-frequency oscillations grows exponentially within the expanding phase interval, and the maximal amplitude is reached at the end of this interval, which is also the phase where – under parameter variation – bubbling becomes visible for the first time. In more sophisticated models of practically relevant circuits, as for example in map (6), they may be truncated by other effects such as saturation. This shows that in such models, saturation is important to prevent high-frequency oscillations from becoming unbounded.

The main purpose of the archetypal model is the investigation of how bubbling is influenced by several parameters of the underlying system. In the present work, we focused on the effect caused by variation of the frequency modulation ratio m. A common expectation is that the quality of signals (in particular, expressed in terms of the total harmonic distortion) improved for increasing m. We demonstrated that this is not always the case and that increasing frequency modulation ratio may cause the onset of bubbling. This counter-intuitive result is easily explained using the archetypal model: Indeed, increasing m causes a linear grow of the length of the expanding phase interval resulting in an exponential growth of the cumulative perturbation amplification factor. We provided an experimental confirmation of this effect.

In addition, using the archetypal model we demonstrated that the onset of bubbling is directly related to the negative derivatives of the functions governing the dynamics on the expanding phase interval. If these derivatives are positive, a different undesired effect may occur, namely a suddenly appearing phase-restricted distortion of the waveforms of the signal not related to high-frequency oscillations. This effect, being caused by the same mechanism as bubbling, shares many of its properties, e.g., its dependency on noise and other parameters.

CRediT authorship contribution statement

Viktor Avrutin: Writing – review & editing, Writing – original draft, Visualization, Validation, Software, Methodology, Investigation, Funding acquisition, Formal analysis, Conceptualization. **Zhanybai T. Zhusubaliyev:** Writing – review & editing, Visualization, Validation, Investigation, Formal analysis, Conceptualization. **Kuntal Mandal:** Writing – review & editing, Writing – original draft, Visualization, Software, Investigation. **Frank Bastian:** Writing – review & editing, Investigation, Conceptualization. **Abdelali El Aroudi:** Writing – review & editing, Writing – original draft, Visualization, Validation, Supervision, Project administration, Methodology, Investigation, Conceptualization.

Declaration of competing interest

The authors declare that they have no known competing financial interests or personal relationships that could have appeared to influence the work reported in this paper.

Acknowledgments

The work of V. Avrutin was supported by the German Research Foundation within the scope of the project “Generic bifurcation structures in piecewise-smooth maps with extremely high number of borders in theory and applications for power converter systems-2” and “Global bifurcation phenomena in discontinuous piecewise-smooth maps in theory and applications for power converter systems”.

The work of F. Bastian was supported by the European Union’s Horizon 2020 Research and Innovation Programmes under the Marie Sklodowska-Curie grant agreement 955708.

K. Mandal acknowledges support from the Agency for Management of University and Research Grants (AGAUR), Spain under the Ministry of Research and Universities of the Government of Catalonia (Grant Reference No. 2020 BP 00260).

The work of Abdelali El Aroudi was supported by the project PID2023-150839OB-I00 financed by MICIU/AEI/10.13039/501100011033, Spain and FEDER, UE, Spain.

Zh.T. Zhusubaliyev was supported by the Ministry of Education and Science of the Russian Federation within the scope of the programme “Implementation of the Strategic Academic Leadership program Priority 2030” (Project No. 1.7.21/4-24-7) and by the Osh State University, Osh, Kyrgyzstan, Grant No 19-24.

Data availability

No data was used for the research described in the article.

References

[1] D. Shmilovitz, On the definition of total harmonic distortion and its effect on measurement interpretation, IEEE Trans. Power Deliv. 20 (1) (2005) 526–528.

[2] I.W. Group, et al., 519-2014-IEEE Recommended Practice and Requirements for Harmonic Control in Electric Power Systems, IEEE Std 519–2014 (Revision of IEEE Std 519–1992), 2014, pp. 1–29.

[3] Y. Chen, C.K. Tse, S. Qiu, W. Schwarz, Coexisting fast-scale and slow-scale instability in current-mode controlled dc/dc converters: analysis, simulation and experimental results, IEEE Trans. Circ. Syst. I 55 (10) (2008) 3335–3348.

[4] H.H.C. Iu, Y. Zhou, C.K. Tse, Fast-scale instability in a PFC boost converter under average current-mode control, Int. J. Circ. Theor. Appl. 31 (2003) 611–624.

[5] X. Wu, C.K. Tse, O. Dranga, J. Lu, Fast-scale instability of single-stage power-factor-correction power supplies, IEEE Trans. Circ. Syst. I (2006) 204–213.

[6] X. Wu, C.K. Tse, S.C. Wong, J. Lu, Fast-scale bifurcation in single-stage PFC power supplies operating with DCM boost stage and CCM forward stage, Int. J. Circ. Theor. Appl. 34 (2006) 341–355.

[7] J. Zou, X. Ma, C.K. Tse, D. Dai, Fast-scale bifurcation in power-factor-correction buck-boost converters and effects of incompatible periodicities, Int. J. Circ. Theor. Appl. 34 (2006) 251–264.

[8] Zh.T. Zhusubaliyev, E. Mosekilde, A.I. Andriyanov, V.V. Shein, Phase synchronized quasiperiodicity in power electronic inverter systems, Phys. D 268 (2014) 14–24.

[9] A. El Aroudi, D. Giaouris, K. Mandal, S. Banerjee, M. Al-Hindawi, A. Abusorrah, Y. Al-Turki, Complex non-linear phenomena and stability analysis of interconnected power converters used in distributed power systems, IET Power Electron. 9 (5) (2016) 855–863.

[10] F. Yang, L. Yang, X. Ma, Fast-scale bifurcation analysis in one-cycle controlled h-bridge inverter, Int. J. Bifurcation Chaos 26 (12) (2016) 1650199.

[11] M. Li, D. Dai, X. Ma, H.H.C. Iu, Fast-scale period-doubling bifurcation in voltage-mode controlled full-bridge inverter, in: Proc. of IEEE Int. Symposium on Circuits and Systems, 2008, pp. 2829–2832.

[12] D.P. Shankar, U. Govindarajan, K. Karunakaran, Period-bubbling and mode-locking instabilities in a full-bridge DC/AC buck inverter, IET Power Electron. 6 (2013) 1956–1970.

[13] W. Lu, S. Lang, L. Zhou, H.H.C. Iu, T. Fernando, Improvement of stability and power factor in PCM controlled boost PFC converter with hybrid dynamic compensation, IEEE Trans. Circ. Sys. I 62 (2015) 320–328.

[14] H. Zhang, Sh. Dong, W. Guan, Y. Liu, Analysis of fast-scale bifurcation in peak current controlled buck-boost inverter based on unified averaged model, Int. J. Bifurcation Chaos 26 (05) (2016) 1650074.

[15] H. Zhang, Sh. Dong, Ch. Yi, W. Guan, Fast-scale non-linear distortion analysis of peak-current-controlled buck–boost inverters, Int. J. Electron. 105 (2) (2018) 274–288.

[16] A. Subramanian, U. Govindarajan, Analysis on the effect of external spurious signals in an h-bridge inverter, IET Power Electron. 11 (11) (2018) 1830–1838.

[17] Y. Han, X. Fang, P. Yang, C. Wang, L. Xu, J.M. Guerrero, Stability analysis of digital-controlled single-phase inverter with synchronous reference frame voltage control, IEEE Trans. Power Electron. 33 (7) (2018) 6333–6350.

[18] S.K. Mazumder, A.H. Nayfeh, D. Boroyevich, An investigation into the fast- and slow-scale instabilities of a single phase bidirectional boost converter, IEEE Trans. Power Electron. 18 (4) (2003) 1063–1069.

[19] V. Avrutin, F. Bastian, Zh.T. Zhusubaliyev, A geometric approach to bubbling, Phys. D 417 (2021) 132808.

[20] V. Avrutin, L. von Schwerin-Blume, Zh.T. Zhusubaliyev, R. Haroun, A. El Aroudi, Noise-induced and border-collision-induced bubbling, Phys. D 435 (2022) 133277.

[21] M. di Bernardo, C.J. Budd, A.R. Champneys. Grazing, Skipping and sliding: analysis of the nonsmooth dynamics of the DC/DC buck converter, Nonlinearity 11 (4) (1998) 858–890.

[22] V. Avrutin, J.D. Morcillo, Zh.T. Zhusubaliyev, F. Angulo, Bubbling in a power electronic inverter: Onset, development and detection, Chaos, Solitons Fractals 104 (2017) 135–152.

[23] Powersim Inc., PSIM: User’s manual, 2020, available online at https://www.powersimtech.com/wp-content/uploads/2021/01/PSIM-User-Manual.pdf. (2021-12-01).

[24] V. Avrutin, Zh.T. Zhusubaliyev, Piecewise-linear map for studying border-collision phenomena in DC/AC converters, Int. J. Bifurcation Chaos 30 (7) (2020) 2030015.

[25] A. El Aroudi, E. Rodriguez, M. Orabi, E. Alarcón, Modeling of switching frequency instabilities in buck-based dc–ac h-bridge inverters, Int. J. Circ. Theor. Appl. 38 (2011) 175–193.